

## Electronic Supplemental Information to: Understanding the Onset of Oscillatory Swimming in Microchannels

Joost de Graaf,<sup>1,\*</sup> Arnold J.T.M. Mathijssen,<sup>2</sup> Marc Fabritius,<sup>1</sup>  
Henri Menke,<sup>1</sup> Christian Holm,<sup>1</sup> and Tyler N. Shendruk<sup>2</sup>

<sup>1</sup>*Institute for Computational Physics (ICP), University of Stuttgart, Allmandring 3, 70569 Stuttgart, Germany*

<sup>2</sup>*The Rudolf Peierls Centre for Theoretical Physics,*

*1 Keble Road, Oxford, OX1 3NP, United Kingdom*

(Dated: May 3, 2016)

### I. SIMULATION DETAILS

In this section we present details of the simulation model that complement the description given in the main text. In addition, we provide further simulation results, which serve to underpin the generality of our findings.

#### A. Fluid Parameters and Swimmer Models

The ‘raspberry swimmers’ are based on the lattice-Boltzmann method implementation [1] and simulated using a graphics processing unit (GPU) based LB solver [2] that is attached to the MD software ESPResSo [3, 4]. This GPU LB employs a D3Q19 lattice and a fluctuating multi-relaxation time (MRT) collision operator [5]. All of our simulations are performed in a quiescent (unthermalized) LB fluid. A three-point interpolation stencil [6] is employed together with the LB viscous coupling of Ref. [7] to couple the raspberry particles to the fluid. We set the fluid density to  $\rho = 1.0m_0\sigma^{-3}$ , the lattice spacing to  $1.0\sigma$ , the time step to  $\Delta t = 0.005\tau$  ( $\tau$  is the time and  $m_0$  the mass unit), the (kinematic) viscosity to  $\nu = 1.0\sigma^2\tau^{-1}$ , and the bare particle–fluid friction to  $\zeta_0 = 25m_0\tau^{-1}$ . Fischer *et al.* [8] provide a detailed description of the dimensionless numbers that specify the fluid properties to which these choices correspond.

We consider two types of self-propelled particles, a rod and cylinder as shown in Fig. S1. The rod consists of nine coupling points spaced  $0.5\sigma$  apart over a line, with  $\sigma$  the LB grid spacing. The cylinder consists of 161 coupling points spread over 23 groups of hexagonal disks (seven particles with distance  $\sigma$ ), stacked alternately with a separation of  $0.5\sigma$  along the axis. The rod has an effective hydrodynamic length of 5.5 and a diameter of 1.7; the cylinder has an effective length of 12 and diameter of 3.2; and the sphere an effective radius of 3.1 [1]. Full details of these swimmers construction (mass, rotational inertia, etc.) are given in Ref. [1].

The raspberry bodies are made into swimmers by assigning a unit (direction) vector  $\hat{p}$  to their center that points along the symmetry axis, see Fig. S1a. This  $\hat{p}$

shape	$v_s$	$\kappa$	$\nu$	$\mu$	$o_1$	$o_2$
rod	$2.5 \cdot 10^{-3}$	$-1.3 \cdot 10^{-2}$	$3.7 \cdot 10^{-2}$	0.0	0.0	-0.11
	$2.5 \cdot 10^{-3}$	$1.3 \cdot 10^{-2}$	$3.7 \cdot 10^{-2}$	0.0	0.0	0.11
cylinder	$9.9 \cdot 10^{-4}$	$-2.7 \cdot 10^{-2}$	0.23	0.0	0.0	-2.1
	$1.0 \cdot 10^{-3}$	$2.7 \cdot 10^{-2}$	0.23	0.0	0.0	2.1

TABLE I. The properties of our LB raspberry swimmers from Legendre-Fourier decomposition [1]. The table provides the shape, the velocity  $v_s$  of the swimmer in units of  $(\sigma/\tau)$ , the dipole strength  $\kappa$  ( $\sigma^3/\tau$ ), the quadrupole strength  $\nu$  ( $\sigma^4/\tau$ ), the source-dipole strength  $\mu$  ( $\sigma^4/\tau$ ), the source octupole  $o_1$  ( $\sigma^5/\tau$ ), and the force octupole  $o_2$  ( $\sigma^5/\tau$ ), respectively. The positive signs of  $\kappa$  correspond to pusher swimmers and the negative ones to pullers.

co-moves with the particle. We apply a force  $\vec{F}$  in the direction of  $\hat{p}$  ( $\vec{F} = F\hat{p}$ ) to the central molecular-dynamics bead, to which the rest of the coupling points are rigidly attached. This force causes the raspberry particle to move. We further apply a counter force  $-\vec{F}$  to the fluid at a position  $l\hat{p}$ , with  $l$  the separation length, to make the system force free. For positive values of  $l$  the swimmer is a puller and for negative values it is a pusher. We refer to Ref. [1] for the specific parameter choices. For convenience, we summarize the relevant quantities that these choices lead to in Table I, namely: the speed and hydrodynamic moments.

Using the size and speed of the swimmers, and kinematic viscosity of fluid, it is clear that Reynolds number of all our swimmers is less than 0.01. We use a quiescent fluid, therefore the Péclet number is ill-defined, as there is no translational (or rotational) diffusion. Both rod- and cylinder-type swimmers model ‘cylindrical’ self-propelled particles, but the level of description varies as well as the speed of the simulation. The rod-like model captures some of the hydrodynamic aspects of an extended object, namely the existence of a hydrodynamic quadrupole. The use of the low number of coupling points makes the simulations fast compared to those for the cylinder swimmer. However, extended objects with a higher coupling-point density, like our cylindrical swimmer, more accurately model a rod-like shape that is impenetrable to the fluid [9]. The use of a cylindrical swimmer thus serves to verify that the results obtained for the rod swimmer are not induced by low coupling-point density.

\* jgraaf@icp.uni-stuttgart.de

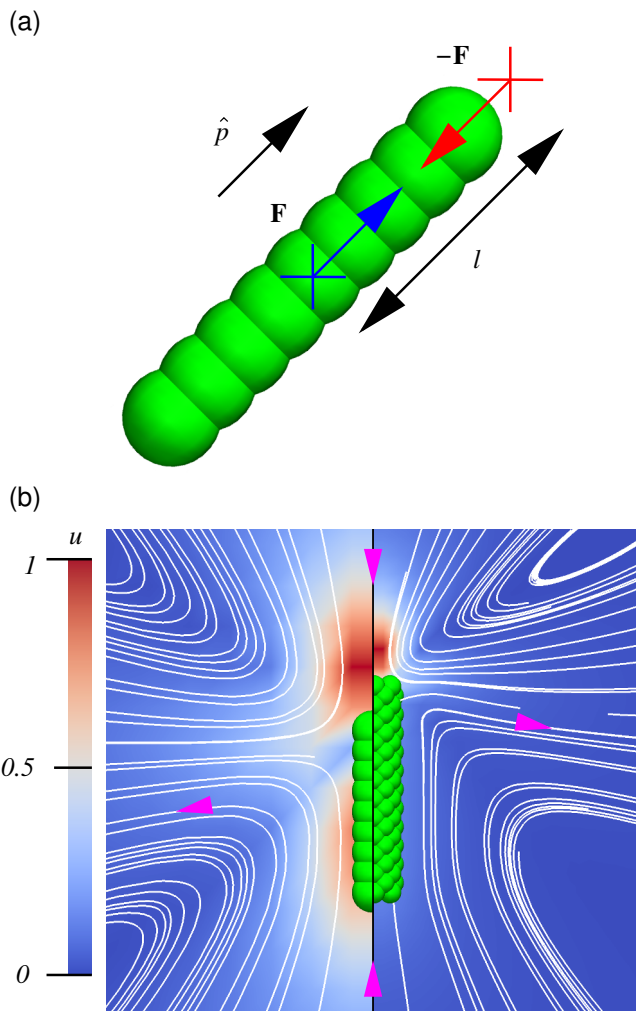


FIG. S1. The flow field around our raspberry-swimmer models. (a) Sketch of a puller-type rod. The size of the green spheres roughly corresponds to the effective hydrodynamic radius of our coupling points ( $\sim 0.5\sigma$ ). A force  $\vec{F}$  (blue arrow) is applied to the central bead (blue cross) in the direction of the symmetry axis  $\hat{p}$  (black arrow). A counter force  $-\vec{F}$  (red arrow) is applied to the fluid at a point  $l\hat{p}$  (red cross), with  $l$  the separation length. (b) The flow field around a puller-type raspberry rod (left) and cylinder (right). The normalized magnitude of the flow velocity in the lab frame given by the legend (red max  $|\vec{u}(\vec{r})| = 1$ , dark blue  $|\vec{u}(\vec{r})| = 0$ ); only a part of the simulation box is shown, again the diameter of the green spheres is  $1\sigma$ . White curves are stream lines and the magenta arrow heads indicate the direction of flow.

## B. Simulation Setup

The above LB and raspberry coupling parameters result in faithful reproduction of theoretical results for passive particles in confining geometries, as was shown by De Graaf *et al.* [10]. Since we use a three-point coupling stencil deviations from the expected behavior of passive particles (solutions to the Stokes' equations) will occur within  $2\sigma$  of the wall, rather than the  $1\sigma$  found

in Ref. [10]. Here, confinement is achieved by placing two no-slip (bounce-back) walls on either side of the simulation box in the  $z$ -direction. We pad the box using two lattice nodes of wall (zero velocity) on either side rather than one, because of the 3-point coupling of our swimmers to the fluid. The simulation domain is kept periodic in the other ( $xy$ ) directions. This leads to a so-called ‘slit-pore’ geometry. We performed Poiseuille flow experiments to verify the height of the channel, the results of which we fit to the Hagen-Poiseuille expression. In all cases, the deviation between the imposed and fitted channel height is minimal ( $\sim 0.1\sigma$ ).

In each of our simulations, the swimmer is initialized in the center of the box in the  $xy$ -direction, at a height  $z$  with respect to the center of the channel ( $z = 0$ ). We ensure that the swimmer's director  $\hat{p}$  is in the  $xz$ -plane and impose its initial angle  $\phi$  with the plate normal  $\hat{z}$ , where  $\phi \in [-\pi/2, \pi/2]$ . Typically, we use  $\phi = 0$  as the initial angle, which means that the swimmer is oriented parallel to the plane. The fluid in the channel is fully quiescent at time  $t = 0$  and the particle starts with zero velocity. The LB parameters are chosen such that after the particle has moved only a fraction of  $\sigma$  the fluid flow field and terminal velocity of the swimmer is established, thereby minimizing the effect of inertia and momentum-transport retardation that physically do not play a role on the colloidal length scale at low Reynolds number.

To prevent the swimmers from penetrating the wall, we include a Weeks-Chandler-Anderson (WCA) interaction between the raspberry coupling points and the bounce-back boundaries. The expression for the interaction is given by

$$U_{\text{WCA}}(r) = \begin{cases} 4\epsilon \left[ \left(\frac{d}{r}\right)^{12} - \left(\frac{d}{r}\right)^6 + \frac{1}{4} \right], & r \leq 2^{1/6}d \\ 0, & r > 2^{1/6}d \end{cases}, \quad (1)$$

where  $r$  is the minimal distance between a coupling point and the wall and  $d$  is the ‘diameter’ of the particle. Every coupling point interacts with the wall via the WCA potential, leading to an overall wall-swimmer interaction that models that of a hard rod or cylinder with a hard wall. We typically use  $d = \sigma$ .

## C. The Angular Evolution for Oscillating Swimmers

For completeness Fig. S2 shows the way the angle  $\phi$  evolves along the trajectory of the swimmers given in Fig. 1 of the main text. The orientation of the rod changes along the trajectory. When the particle moves between the two walls, it comes close to making a  $45^\circ$  angle with respect to the horizontal. This is further visualized in the supplemental movies described in the next section.

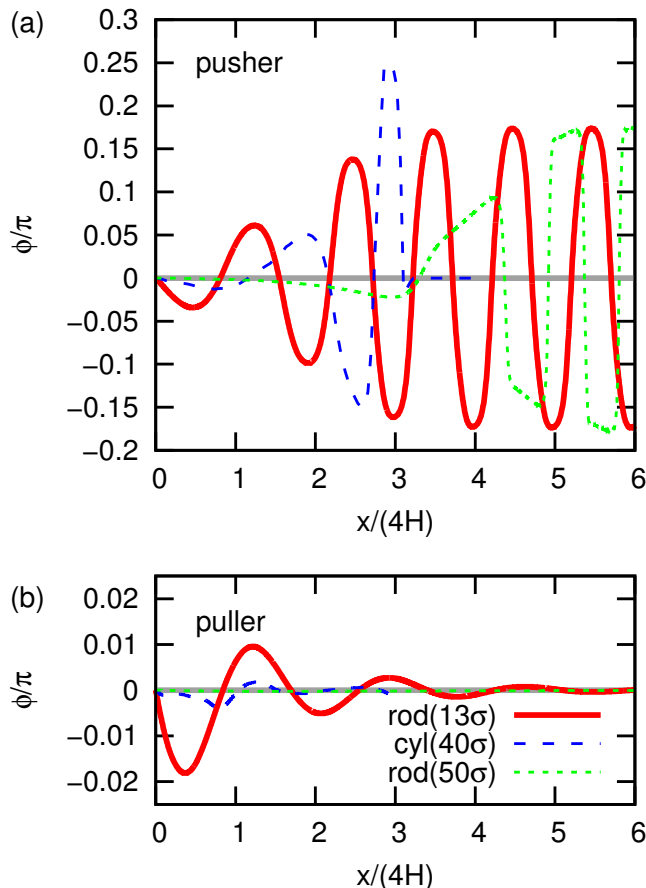


FIG. S2. The angle  $\phi$  as a function of horizontal displacement  $x$  of swimmers between two parallel plates with separation  $H$ . Results are for swimmers that are initially oriented parallel to the walls and at  $z = 1\sigma$ ; using the exact same data sets as used in Fig. 1 of the main text. (a) The results for pushers: rod for  $H = 13\sigma$  (red, solid), cylinder for  $H = 40\sigma$  (blue, dashed), and rod for  $H = 50\sigma$  (green, dots). (b) The results for pullers, otherwise the systems are the same.

#### D. Description of the Supplemental Movies

To illustrate the movement of the swimmers, we have included two movies in the ESI. These show the trajectory of a puller and pusher rod in a confining channel with height  $H = 13\sigma$  and lateral extent  $L = 70\sigma$ . The initial position is  $z = 1\sigma$  and  $\phi = 0$  and we used a WCA parameter of  $d = \sigma$ . The labeling of the movies is as follows: the type of the particle is given, followed by a list of quantities and values, with each set separated by a double underscore. The notation of the quantities is the one used throughout and each quantity and value are separated by a single underscore. We chose a slightly smaller lateral extent of the channel than used to produce Fig. 1 of the main text. The reason is that for the typical channel sizes studied in our work, the motion of the swimmer would be difficult to observe. However, we have verified that the limited size of the channel does not strongly effect the trajectory.

#### E. LB Algorithm Limitations in the Near-wall Region

We scrutinize the presence of the artificial limit cycle for our pusher-type rod through a series of computational examinations. By our examinations we reach the following conclusions. Since the LB algorithm does not explicitly account for near-wall lubrication corrections [8], it fails to be accurate in the near wall regime and we are therefore unable to comment on the nature of any potential limit cycle. Additionally, the counter-force point can artificially penetrate the wall at the point of closest approach. These points indicate that, although limit cycles may exist in certain physical swimmers, the simulated trajectories cannot offer physically relevant predictions. We explain the way we arrived at these conclusions in detail below.

In our examination of the system, the lateral extent of the domain is varied between  $L = 5H$  and  $L = 35H$  to eliminate the effect of  $xy$  periodicity on our results: there is no discernible impact of  $L$  on the trajectories above  $L = 10H$ . We vary the viscosity and swimming speed to verify that retardation of the fluid momentum transport does not introduce these cycles; these changes only have a small effect. The value of the WCA interaction  $d$  is varied, as shown explicitly in Fig. S3. We find that for  $d > 1.5\sigma$  the limit cycle disappears and the rod's trajectory is reminiscent of the pusher cylinder's, see Fig. 1 in the main text. In both of these cases (inflated WCA rod and the unmodified cylinder) non-hydrodynamic contact with the WCA wall occurs and the self-propelled particles move along the plane of contact (sliding). Similar sliding dynamics have been observed in simulations that neglect HIs [11].

The pusher rod performs its persistent oscillatory trajectory even in the absence of the WCA potential. Fortunately, it does not penetrate the wall, although penetration can be achieved in this case by starting with values of  $\phi$  that are greater than  $\sim 25^\circ$  when  $d = 0$ . This may seem to indicate that the limit cycle is a physical effect. However, this is not the case, as the rod comes very close to the wall, where LB does not faithfully reproduce hydrodynamics [10].

We therefore also considered the interaction of the counter-force point with the wall, see Fig. S4. We find that the counter-force interpolation (which takes place over a region of  $3\sigma$  in diameter due to the three-point coupling) is partially inside of the wall at the closest approach, which impacts the reorientation of the rod. To check the effect of this, we switched to a two-point interpolation stencil. The limit cycle persists, but here too the interpolation region overlaps with the wall nodes, even though the overlap is substantially reduced. When the value of  $d$  increases beyond  $d = 1.5\sigma$ , the counter-force point is no longer interpolated inside the wall. Similarly, the cylinder's size prevents its counter-force point from being interpolated into the wall at closest approach. This indicates that the limit cycle observed for LB-raspberry

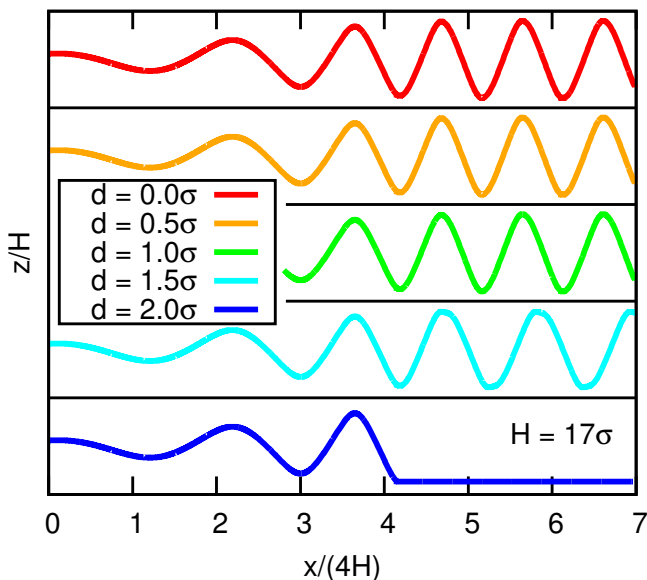


FIG. S3. Trajectories of pusher-type rods between two parallel plates with separation  $H = 17\sigma$ . The horizontal displacement  $x$  and vertical position  $z$  are given for a swimmer that is initially oriented parallel to the walls  $\phi = 0$  and at  $z = 1\sigma$ , with  $\sigma$  the MD unit of length and  $z = 0$  the center of the channel. For each curve, the top of the black frame enclosing the trajectory is at  $z/H = 1/2$ , while the bottom is at  $z/H = -1/2$ . From top to bottom, the range of the WCA interaction  $d$  increases from 0 to  $2\sigma$  in steps of  $0.5\sigma$ .

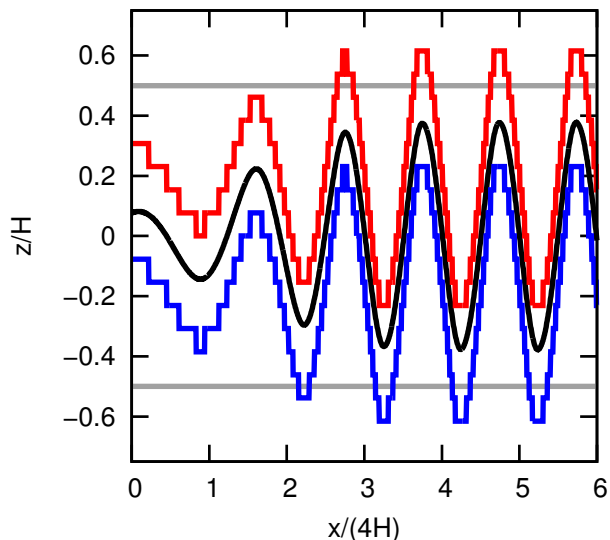


FIG. S4. Trajectory (black curve) of a pusher-type rod between two parallel plates (gray lines) with separation  $H = 13\sigma$ . The horizontal displacement  $x$  and vertical position  $z$  are given for a swimmer that is initially oriented parallel to the walls  $\phi = 0$  and at  $z = 1\sigma$ , with  $\sigma$  the MD unit of length and  $z = 0$  the center of the channel. The vertical extent of the lattice nodes involved in the 3-point interpolation of the counter-force are indicated using the red and blue lines.

swimmers is due to limitations in simulating the hydrodynamic interactions for close swimmer-wall separations, because of the spread-out counter-force scheme.

While the near-wall hydrodynamics are not accurately captured by our algorithm, the far-field is. Therefore, in a system where there is a long-range (non-hydrodynamic) repulsion, our algorithm would produce the correct physics — provided that the range of the repulsion is sufficient to keep the LB coupling points far enough away from the wall. In the main text, we chose the WCA repulsion in such a way that the size of the ‘hard core’ matches the effective hydrodynamic size of the particle. Choosing the WCA range much larger, would remove this physical correspondence; therefore using an additional soft potential would be more appropriate to achieve wall repulsion. We are, however, unaware of any biological or artificial swimmers that are strongly repulsed from boundaries by long-ranged potentials and have therefore not considered this possibility further here.

In summary, the persistent oscillation (limit cycle) seen after long times for pusher-type swimmers must be attributed to a simulation artifact. Nevertheless, for the onset of the oscillation, which we are interested in the main text, there are no counter-force-overlap problems, as is clearly illustrated in Fig. S4.

## F. Rod Swimmer Length

The effect of rod length on the trajectories of pushers is seen in Fig. S5. Since the effective hydrodynamic diameter of the rods is governed primarily by the coupling parameters when using only a single row of coupling points [9], varying the length has the effect of varying the aspect ratio of rod-shaped particles. We found only minor modifications of the trajectories, reflecting the minor changes in the hydrodynamic multipole expansion due to the change in aspect ratio. That is, the presence of a hydrodynamic quadrupole is the dominant effect in the formation of oscillatory trajectories; the strength of the quadrupole moment is only weakly perturbed by the changes in the length that we considered.

## G. Helical Trajectories

The LB-raspberry swimmer model can be extended to simulate swimmers in other geometries. We find that our rods display helical trajectories, see Fig. S6. The helical trajectory observed for a tube with a square cross section is due to the swimmer starting off-center and away from one of the symmetry planes. Puller rods move consistently towards the center of the tube (not shown here) and also exhibit helical motion. The helical trajectory of the swimmer in the circular tube is due to a numerical artifact close to the boundary. The first part of the trajectory in the circular tube is purely oscillatory, as expected on the basis of symmetry and as we also observed

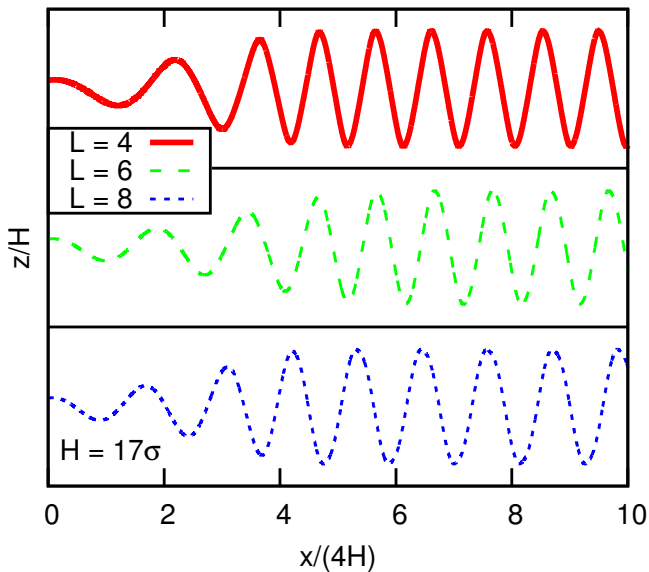


FIG. S5. The  $(x, z)$  trajectories for pusher rods confined to a channel of height  $H = 17\sigma$ , which have initial position  $z = 1\sigma$  and angle  $\phi = 0$ . We vary the length of the rod by adding coupling points. The rod used throughout has a bare length of  $4\sigma$  (solid red curve) [and an effective hydrodynamic length of  $5.5\sigma$ ]. Puller rods with bare length 6 (green dashed) and 8 (blue short dashes) are also shown. For each curve, the top of the black frame enclosing the trajectory is at  $z/H = 1/2$ , while the bottom is at  $z/H = -1/2$ .

for pullers. Only when an initial yaw angle is imposed does the rod perform a helical trajectory from the start of the simulation, similar to the observations of Ref. [12].

## II. SWIMMER-GENERATED FLOW FIELDS

As a swimmer at position  $\vec{r}$  and orientation  $\hat{p}$  moves, it disturbs the surrounding bulk fluid at position  $\vec{x}$ . This disturbance field can be written in terms of a multipole expansion

$$\vec{u}(\vec{x}, \vec{r}, \hat{p}) = \kappa \vec{u}_D + \nu \vec{u}_Q + \mu \vec{u}_{SD} + o_1 \vec{u}_{O_1} + o_2 \vec{u}_{O_2} + \dots \quad (2)$$

where  $\vec{u}_D$  is the Stokes dipole representing the opposing propulsion and drag forces,  $\vec{u}_Q$  the quadrupole representing the fore-aft asymmetry of the swimmer,  $\vec{u}_{SD}$  the source doublet representing the finite size of the swimmer, and the octupolar terms  $\vec{u}_{O_1}$  and  $\vec{u}_{O_2}$  describe the features of the flow in more detail [13]. Possible Stokeslet and rotlet (doublet) terms are omitted as the raspberry swimmers are force and torque free.

These Newtonian flow fields can be written in terms of derivatives of the Oseen tensor

$$\mathcal{J}_{ij}(\vec{r}) = \frac{\delta_{ij}}{R} + \frac{R_i R_j}{R^3}, \quad (3)$$

where  $i, j \in \{x, y, z\}$  are indices. This produces a point-force Stokeslet  $u_i^S = p_j \mathcal{J}_{ij}$  velocity field at position  $\vec{x}$  due

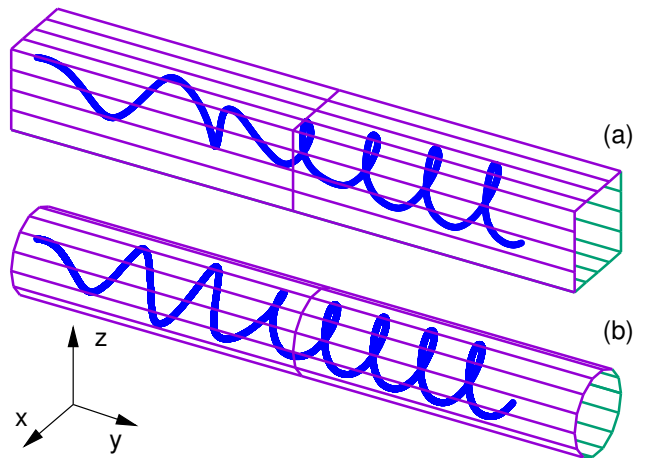


FIG. S6. Trajectory (blue curve) of a pusher-type rod in a square tube (a) and a circular tube (b). The side length/diameter is  $H = 17\sigma$ . The swimmer is initially oriented parallel to the walls  $\phi = 0$  and located at  $x = 2\sigma$  and  $z = 1\sigma$ , with  $\sigma$  the MD unit of length and  $x = z = 0$  the center of the tube. The trajectories shown here are  $28H$  long in the  $y$  direction.

to a point force at position  $\vec{r}$ ; where  $\delta_{ij}$  is the Kronecker delta and  $R = |\vec{x} - \vec{r}|$ . From this [13] we obtain

$$\vec{u}_D(\vec{x}, \vec{r}, \hat{p}) = +(\hat{p} \cdot \vec{\nabla}) \vec{u}^S, \quad (4)$$

$$\vec{u}_Q(\vec{x}, \vec{r}, \hat{p}) = -\frac{1}{2}(\hat{p} \cdot \vec{\nabla})^2 \vec{u}^S, \quad (5)$$

$$\vec{u}_{SD}(\vec{x}, \vec{r}, \hat{p}) = -\frac{1}{2} \nabla^2 \vec{u}^S, \quad (6)$$

$$\vec{u}_{O_1}(\vec{x}, \vec{r}, \hat{p}) = +\frac{1}{6} \nabla^2 (\hat{p} \cdot \vec{\nabla}) \vec{u}^S, \quad (7)$$

$$\vec{u}_{O_2}(\vec{x}, \vec{r}, \hat{p}) = +\frac{1}{6} (\hat{p} \cdot \vec{\nabla})^3 \vec{u}^S, \quad (8)$$

where the derivatives act on the swimmer position  $\vec{r}$ . Hence, inserting equations (4–8) into (2) gives the swimmer-generated flow field in the absence of walls.

### A. Wall-Induced Hydrodynamic Interactions

These flow fields must be modified in the vicinity of boundaries. This can be done by the method of images so that the no-slip boundary conditions of both walls are satisfied. Consider the upper wall (denoted by superscript +): an additional velocity  $\vec{u}^+$  must be added to the multipole expansion velocity  $\vec{u}$  from (2) in order to satisfy the no-slip boundary condition at the wall  $z = H/2$ . We write this as  $[\vec{u} + \vec{u}^+]_{z=H/2} = 0$ . Likewise, the same is true at the bottom wall (denoted by superscript -) and we say  $[\vec{u} + \vec{u}^-]_{z=-H/2} = 0$ . The two velocity fields  $\vec{u}^\pm$  represent an image system for the upper and lower wall, respectively. For two parallel walls the image system comprises an infinite series of images, but we consider only the first two images in this ESI. This derivation can be extended to  $N$  images [14], and the results reported in the main text use eight images (four for each wall).

These two images (above the upper wall [+ ] and below the lower [- ]) are located at position

$$\vec{r}^\pm = \pm(H/2)\hat{e}_z + \underline{\underline{M}}(\mp(H/2)\hat{e}_z + \vec{r}) \quad (9)$$

where  $\underline{\underline{M}} = \text{diag}(1, 1, -1)$ . Hence, the relative distance between the images and a point in the fluid is  $\vec{R}^\pm = \vec{x} - \vec{r}^\pm$ . The velocity field of the image flow is then given by the Blake tensor in index notation

$$\mathcal{B}_{ij}^\pm = \left( -\delta_{jk} + 2h^\pm \delta_{kz} \partial_j + (h^\pm)^2 M_{jk} \nabla^2 \right) \mathcal{J}_{ik}, \quad (10)$$

where  $h^\pm = \frac{1}{2}(\vec{r} - \vec{r}^\pm) \cdot \hat{e}_z$ , derivatives are taken with respect to swimmer position, and repeated indices are summed over. The two image systems due to point forces in the direction  $\hat{p}$  are then  $p_j \mathcal{B}_{ij}^\pm$ . From this pair of Stokeslet images, the image systems of the Stokes dipole, quadrupole, *etc.* can be constructed accordingly by taking successive derivatives as in equations (4–8) and the complete image system for the pair  $\vec{u}^\pm$  is found.

These image velocity fields interact hydrodynamically with the swimmer. The wall-induced translational and rotational velocities of the force-free and torque-free swimmer are found by rearranging the Faxén relations evaluated at the swimmer position. Hence, we have

$$\vec{v}_h = \left[ \left( 1 + \frac{1}{8} a^2 \nabla^2 \right) \vec{u}^\pm \right]_{\vec{x}=\vec{r}}, \quad (11)$$

$$\vec{\Omega}_h = \left[ \frac{1}{2} \vec{\nabla} \times \vec{u}^\pm + G \hat{p} \times (\underline{\underline{E}}^\pm \cdot \hat{p}) \right]_{\vec{x}=\vec{r}}, \quad (12)$$

where the derivatives act on the position  $\vec{x}$ ,  $\underline{\underline{E}}$  is the rate-of-strain tensor,  $a$  is characteristic size of the swimmer, and  $G = \frac{\gamma^2 - 1}{\gamma^2 + 1}$  is a function of the aspect ratio  $\gamma$ . Inserting the images of the swimmer-generated flow field (2) into the Faxén relations (11–12) yields the wall-induced advection and rotation ( $\vec{v}_{\text{HI}}$  and  $\vec{\Omega}_{\text{HI}}$  in the equations of motion of the main text).

### III. SWIMMER DYNAMICS MODEL

Using the translational invariance along the  $x$  and  $y$  directions, we write the swimmer's orientation as  $\hat{p} = (\cos \phi, 0, \sin \phi)$  without loss of generality, where  $\phi = 0$  corresponds to swimming parallel to the walls. Hence, the swimmer's equations of motion simplify to the two coupled equations,  $\dot{\phi} = \dot{\phi}(\phi, z)$  and  $\dot{z} = \dot{z}(\phi, z)$ . If we consider the simplified case of a point swimmer with aspect ratio  $\gamma = 1$ , and only use one image system on each side of the channel, these equations are

$$\dot{\phi} = \pm \frac{3\kappa \sin 2\phi}{16(z \mp \frac{H}{2})^3} \mp \frac{3\nu(\cos \phi + 3 \cos 3\phi)}{64(z \mp \frac{H}{2})^4} \mp \frac{3\mu \cos \phi}{8(z \mp \frac{H}{2})^4} \mp \frac{o_1 \sin 2\phi}{4(z \mp \frac{H}{2})^5} \mp \frac{3o_2(14 \sin 2\phi + 15 \sin 4\phi)}{512(z \mp \frac{H}{2})^5}, \quad (13)$$

$$\dot{z} = \pm \frac{3\kappa(3 \cos 2\phi - 1)}{16(z \mp \frac{H}{2})^2} \pm \frac{\nu(\sin \phi + 9 \sin 3\phi)}{32(z \mp \frac{H}{2})^3} \pm \frac{\mu \sin \phi}{(z \mp \frac{H}{2})^3} \mp \frac{5o_1(3 \cos 2\phi - 1)}{32(z \mp \frac{H}{2})^4} \mp \frac{15o_2 \cos^2 \phi(5 \cos 2\phi - 3)}{128(z \mp \frac{H}{2})^4} + v_s \sin \phi. \quad (14)$$

#### A. Fitting Hydrodynamic Moments

An extension of these equations of motion (13–14), with  $a \neq 0$  and  $G \neq 0$ , is used to match the dynamics of the model swimmers and LB swimmers (Table 1; main text). To achieve this, the time derivatives  $\dot{\phi}$  and  $\dot{z}$  are extracted from the LB trajectories for a number of randomly chosen  $(\phi, z)$  coordinate points,  $N = 500$ . Note that the first point in time is chosen to be after the first half oscillation such that the LB-raspberry swimmer has reached a constant swimming velocity and retardation effects are minimized. At each point, the LB values are compared to the values predicted by the model with

a least squares method:

$$S = \sum_{i=1}^N \frac{(\dot{\phi}_{\text{LB}} - \dot{\phi}_{\text{model}})^2}{(2\pi)^2} + \frac{(\dot{z}_{\text{LB}} - \dot{z}_{\text{model}})^2}{H^2}. \quad (15)$$

Hence, the theory and LB simulations are matched by minimizing the  $S$  function with respect to the far-field multipole expansion parameters. Here, the swimming speed  $v_s$  is fixed at the actual values (Table 1; main text). Likewise, the particle radius  $a$  is chosen to be fixed at the half-length of the LB rod or cylinder swimmer and the aspect ratio  $\gamma$  is set to its geometric value. Similarly, the parameters  $\mu, o_1$  are constrained to the LB-measured values, which is physically reasonable because these source doublets and quadrupoles are expected to be comparatively small, since our swimmers are constructed without fluid sources or sinks [1]. Finally, the multipole moments

$\kappa, \nu, o_2$  are allowed to vary, where a standard simulated annealing algorithm is used to find the least squares.

### B. Analysis of swimmer oscillations

In order to analyze the micro-swimmer dynamics, we linearize the equations of motion (13–14) about the centerline of the micro-channel ( $z = 0$ ), and about the orientation parallel to the walls ( $\phi = 0$ ). For simplicity, we consider only the dipolar and quadrupolar contributions to the multipole expansion and set the octupolar and higher-order contributions to zero. The dynamics can then be captured by the matrix equation

$$\begin{pmatrix} \dot{\phi}(t) \\ \dot{z}(t) \end{pmatrix} = \begin{pmatrix} -\frac{6\kappa}{H^3} & -\frac{48(\nu + 2\mu)}{H^5} \\ v_s - \frac{2(7\nu + 8\mu)}{H^3} & \frac{12\kappa}{H^3} \end{pmatrix} \begin{pmatrix} \phi \\ z \end{pmatrix}. \quad (16)$$

First, we consider the motion in the absence of a dipole moment ( $\kappa = 0$ ), but with quadrupole moment  $\nu$  and source doublet moment  $\mu$ . Then, the eigenvalues  $\lambda_e$  of the matrix are

$$\lambda_e = \pm \frac{4\sqrt{3(\nu + 2\mu)(14\nu + 16\mu - v_s H^3)}}{H^4}, \quad (17)$$

which corresponds to oscillatory motion ( $\lambda_e$  is imaginary) if  $H > ([14\nu + 16\mu]/v_s)^{1/3}$ . That is to say that the channel must be wide enough with respect to  $\nu, \mu$ , and the swimming speed  $v_s$  in order to observe oscillatory motion. For channels that are narrower than the critical height  $H_c = ([14\nu + 16\mu]/v_s)^{1/3}$  the theory pre-

dicts that the swimmers do not oscillate. For our oscillating LB-raspberry swimmers this condition is met (Table 1; main text). Specifically, for the rod-type swimmer, we measured  $\nu = 3.7 \cdot 10^{-2} \sigma^4/\tau$ ,  $\mu = 0 \sigma^4/\tau$  and  $v_s = 2.5 \cdot 10^{-3} \sigma/\tau$ . Therefore, condition for oscillatory motion is satisfied for channels heights  $H_c \simeq 6$ . Similarly for the cylinder-type LB swimmer, we find oscillatory motion requires  $H_c \simeq 14$ . In our simulations, we use channels heights that are larger than these critical values.

Hence, oscillatory dynamics can be observed. With the initial conditions  $z(0) = z_0$  and  $\phi(0) = 0$ , the swimmer's position in the channel is given by  $z(t) \approx z_0 \cos(\omega t)$ , where the oscillation frequency

$$\omega = i\lambda_e \approx 4\sqrt{\frac{3\nu v_s}{H^5}} \quad (18)$$

tends to zero as  $\nu \rightarrow 0$  or  $H \rightarrow \infty$ , so that the oscillations gradually disappear in large channels.

With  $\kappa$  included, the eigenvalues of equation (16) are

$$\lambda_e = \frac{3\kappa}{H^3} \pm i\omega \equiv \alpha \pm i\omega, \quad (19)$$

$$\omega^2 = \frac{48v_s(\nu + 2\mu)}{H^5} - \frac{81\kappa^2}{H^6} - \frac{96(\nu + 2\mu)(7\nu + 8\mu)}{H^8}, \quad (20)$$

where we have introduced  $\alpha = 3\kappa/H^3$ . Therefore, provided  $\omega^2 > 0$ , the swimmer dynamics can be approximated by

$$z(t) \approx z_0 \cos(\omega t) \exp(\alpha t), \quad (21)$$

which describes oscillatory trajectories, growing in amplitude for pushers and decreasing for pullers.

- 
- [1] J. de Graaf, H. Menke, A. Mathijssen, M. Fabritius, C. Holm and T. Shendruk, *J. Chem. Phys.*, 2016, **144**, 134106.
- [2] D. Roehm and A. Arnold, *Eur. Phys. J. ST*, 2012, **210**, 73.
- [3] H. J. Limbach, A. Arnold, B. A. Mann and C. Holm, *Comp. Phys. Comm.*, 2006, **174**, 704.
- [4] A. Arnold, O. Lenz, S. Kesselheim, R. Weeber, F. Fahrenberger, D. Roehm, P. Kořovan and C. Holm, *Meshfree Methods for Partial Differential Equations VI*, 2013, p. 1.
- [5] D. d'Humières, I. Ginzburg, M. Krafczyk, P. Lallemand and L.-S. Luo, *Philos. Trans. A Math. Phys. Eng. Sci.*, 2002, **360**, 437.
- [6] A. Ladd, *J. Fluid Mech.*, 1994, **271**, 285.
- [7] P. Ahlrichs and B. Dünweg, *J. Chem. Phys.*, 1999, **111**, 8225.
- [8] L. Fischer, T. Peter, C. Holm and J. de Graaf, *J. Chem. Phys.*, 2015, **143**, 084107.
- [9] J. de Graaf, G. Rempfer and C. Holm, *NanoBioscience, IEEE Transactions on*, 2015, **14**, year.
- [10] J. de Graaf, T. Peter, L. Fischer and C. Holm, *J. Chem. Phys.*, 2015, **143**, 084108.
- [11] J. Elgeti and G. Gompper, *Euro. Phys. Lett.*, 2009, **85**, 38002.
- [12] L. Zhu, E. Lauga and L. Brandt, *J. Fluid Mech.*, 2013, **726**, 285.
- [13] A. J. T. M. Mathijssen, D. O. Pushkin and J. M. Yeomans, *J. Fluid Mech.*, 2015, **773**, 498.
- [14] A. Mathijssen, A. Doostmohammadi, J. Yeomans and T. Shendruk, *J. R. Soc. Interface*, 2016, **13**, 1742.